

Single-shot Specular Surface Reconstruction with Gonio-plenoptic Imaging

Lingfei Meng
Ricoh Innovations, Corp.
meng@ric.ricoh.com

Liyang Lu*
Rice University
liyang.lu@rice.edu

Noah Bedard, Kathrin Berkner
Ricoh Innovations, Corp.
{noah,berkner}@ric.ricoh.com

Abstract

We present a gonio-plenoptic imaging system that realizes a single-shot shape measurement for specular surfaces. The system is comprised of a collimated illumination source and a plenoptic camera. Unlike a conventional plenoptic camera, our system captures the BRDF variation of the object surface in a single image in addition to the light field information from the scene, which allows us to recover very fine 3D structures of the surface. The shape of the surface is reconstructed based on the reflectance property of the material rather than the parallax between different views. Since only a single-shot is required to reconstruct the whole surface, our system is able to capture dynamic surface deformation in a video mode. We also describe a novel calibration technique that maps the light field viewing directions from the object space to subpixels on the sensor plane. The proposed system is evaluated using a concave mirror with known curvature, and is compared to a parabolic mirror scanning system as well as a multi-illumination photometric stereo approach based on simulations and experiments.

1. Introduction

Measuring the geometry of surfaces is an active research topic, and has many applications, such as realistic image rendering [6] and surface inspection [19]. Estimating the geometry for a specular surface is still a challenging problem in the field of computer vision [23], and most dense shape reconstruction techniques assume the scene to be Lambertian [7]. Recently new techniques have been proposed to address measurement of specular surfaces. In general, a large number of image acquisitions are required [6, 7, 23], or the surface needs to be pressed into an elastomeric sensor with known reflectivity [10, 11]. Estimating surface normals from a single image is still a challenging and open research problem.

Whereas disparity-estimation based methods from data

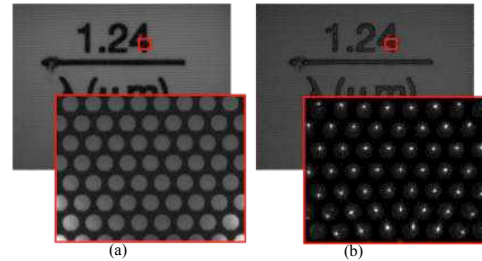


Figure 1. Raw sensor images captured by our plenoptic camera on a flat plastic ruler card (a) in ambient room light condition, and (b) with collimated illumination.

obtained with a stereo imaging system uses only two views, plenoptic cameras, in comparison, enable capture of a 4D light field in a single-shot for depth estimation [1, 20, 22]. Depth estimation of objects using a plenoptic camera typically relies on the parallax between different views captured by the camera, similarly to conventional stereo imaging. In a plenoptic imaging system, images are commonly captured with flat field illumination or any regular illumination, such as ambient illumination without specifically controlled directionality. Using such a illumination scheme, a plenoptic camera cannot resolve very fine 3D structures of a surface due to limited depth resolution of the system, or estimate the geometry of a textureless surface due to the absence of features necessary for disparity estimation.

In this paper we present a *gonio-plenoptic imaging system* that realizes a single-shot shape measurement for specular surfaces that contain very fine or textureless 3D structures in a micron-scale. Besides, our system is able to capture dynamic surface deformation in a video mode. Similar to a goniophotometer our system measures the light at different angles, but only one image acquisition is required. Our system is comprised of a collimated illumination and a plenoptic camera. In contrast to a conventional plenoptic camera, our system does not rely on the parallax between multiviews; instead the shape of a surface is reconstructed based on the reflectivity of the surface. The use of a collimated illumination source allows us to capture the bidirectional reflectance distribution function (BRDF) variation of the surface, which is used as a cue for surface geometry

*Liyang Lu performed the work while at Ricoh Innovations, Corp..

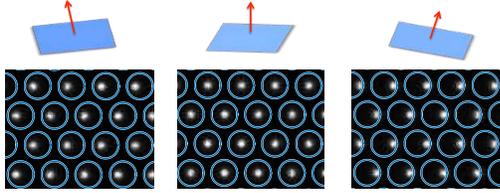


Figure 2. Plenoptic images captured on a mirror surface with its surface normal changed.

estimation. To illustrate this we first present a raw sensor image captured by our plenoptic camera in ambient room light condition in Figure 1 (a). The image is of a flat plastic ruler card placed at the focal plane of the camera. The bottom image is a magnification of the area within the rectangle in the top image. Each circle in the bottom image is a separate superpixel formed by one microlens. Light gathered in each superpixel is approximately uniform because the object was illuminated from many directions. In this case there is no indication about the shape of the surface. Figure 1 (b) shows another raw sensor image that was captured by the same plenoptic camera at the same object distance, but with collimated illumination. It can be seen that each superpixel contains a peak caused by the specular reflection of the collimated illumination, which is an important cue for surface normal estimation. Figure 2 further explains the dependency of the peak on the surface normal of the object. When the surface normal is oriented to different directions, the response of the superpixel also changes because the direction of the specular reflection changes. In this example, the peak location within the superpixel is an indication of the specular reflection, which is also an indication of the surface normal.

2. Related Work

Specular Surface Measurement

In the earlier work of photometric stereo the reflectance of surface was required to be Lambertian [2, 26]. Recently the conventional photometric stereo techniques have been extended to specular surfaces with varying BRDFs. Hertzmann et al. [7] presented an example-based photometric stereo method by placing a reference target in the scene and finding the correspondence between the observed data and the target. In their experiment the measured sample objects were required to be composed of the same material as the reference target. Goldman et al. [6] proposed a photometric stereo method for surfaces with spatially-varying BRDF. They modeled the surface reflectance as a linear combination of fundamental materials, and recovered the shape, material BRDF, and weight maps using the well-known Ward model. In their experiment 12 images were taken under different illumination directions in order to solve the

non-linear equation. In [5] the spatially-varying reflectance properties of a surface is obtained based on a single pass of a linear light source.

A large body of work deals with specular surface reconstruction based on shape from specularity technique. Nayar et al. [16] presented a specular surface inspection method using an array of point sources. Wang and Dana proposed a device with a concave parabolic mirror to view multiple angles on specular surfaces [23]. A beam of light parallel to the optical axis illuminates a point on the sample, and a subset of the hemisphere of outgoing light is reflected by the mirror and captured in a single photo. Each time a single point was measured and the whole surface was scanned by moving the mirror with a translation stage. For points with near-specular reflectance, this image will have a strong peak at the specular direction thus yielding the point's surface normal. A relief image was then reconstructed. Our approach uses the same principle as Wang and Dana's that the hemisphere of radiance is captured in a single-shot. However, in Wang and Dana's system in order to measure 200×200 points 40,000 images need to be collected. Chen et al. [3] presented a method using hand-held illumination to recover translucent and highly specular objects. Francken et al. [4] measured mesostructure from specularity using a LCD monitor and a digital camera. Some other approaches use multiple views to reconstruct shape of specular surfaces [9, 27]. All these methods provide new ways to reconstruct the shape of a specular surface; however, they still require a large number of images to be acquired.

Johnson and Adelson [10, 11] presented a method for measuring material texture and shape in a single image by using an elastometric sensor. In their system the object was pressed into an elastomer skin with known BRDF, and photometric stereo was used based on multiple colored light coming from different directions. Using the known reflectance of the covered skin, specularity of the measured surface was removed. However, the surface needs to be contacted by the skin and the reflectivity of the surface is completely lost using this approach.

Plenoptic Camera/Light Field Imaging

A plenoptic camera uses a microlens array to capture the 4D light field information from the scene. Adelson and Wang [1] presented a single lens stereo system using a plenoptic camera. Depth information was recovered based on the horizontal and vertical parallax. The technology was further extended by Ng et al. [18], who developed a hand-held plenoptic camera for image refocusing. Levoy et al. [12] also demonstrated a prototype light field microscope, which can be used to reconstruct 3D volumes of biological specimens. By inserting a second microlens array into the microscope's illumination path Levoy et al. [13] also controlled directions of the illumination. Lumsdaine and

Georgiev [14] developed a focused plenoptic camera to increase the spatial resolution. Perwaß and Wietzke [20] extended the depth-of-field and effective resolution of plenoptic camera by using a microlens array with three different focal lengths. Among these approaches the objects in the scene need to be presented at varying depths in order to capture sufficient parallax between different views. However, when a flat surface with very fine 3D structure is at a single depth plane or a surface is textureless a plenoptic camera is not able to reconstruct the shape of the surface, because all the current approaches rely on parallax in the captured data to calculate disparities. In addition to plenoptic imaging, light field probes or coded collimated illumination were used to capture refractive shape of transparent objects and gas flows [8, 15, 25]. Our work is also closely related to Shack-Hartmann wavefront sensor, which uses lenslet array to image the aberrated wavefront down to spots on a sensor array and the deviation of these spots with respect to a reference is used to characterize the aberration of wavefront [21]. Rather than measuring the wavefront we capture BRDF and reconstruct much finer surface geometry.

Our method is closely related to the work in specular surface measurement and light field imaging. But our technology overcomes some of the limitations that existed in prior work, such as requiring a large number of images to be captured, relying on complicated mechanical translation, or incapable of measuring fine-scale geometry of surfaces by using general plenoptic imaging. To the best of our knowledge, our gonio-plenoptic imaging system is the first of its kind that is able to reconstruct fine-scale geometry of a specular surface in a single-shot. Furthermore, the unique feature of our system enables measuring dynamic surface deformation in video mode. We also introduced a novel object space calibration technique which is an important task in plenoptic imaging system engineering.

3. Methods

3.1. Imaging System

The schematic diagram of our gonio-plenoptic imaging system is shown in Figure 3 (a), and our bench setup is presented in Figure 3 (b). For convenience the imaging optics are depicted in Figure 3 (a) as a single objective lens without showing the multiple elements. Collimated LED illumination is coupled into the system using a beam splitter. A beam-expanding lens system is used to expand the input beam to cover the whole field of view of the camera. The illumination direction is fixed to be parallel to the optical axis. For an illuminated point on the object, the radiance distribution of the reflected light over different viewing directions is captured by the main lens. A microlens array is located at the imaging plane, and each microlens images the aperture of the main lens. Each microlens images the rays

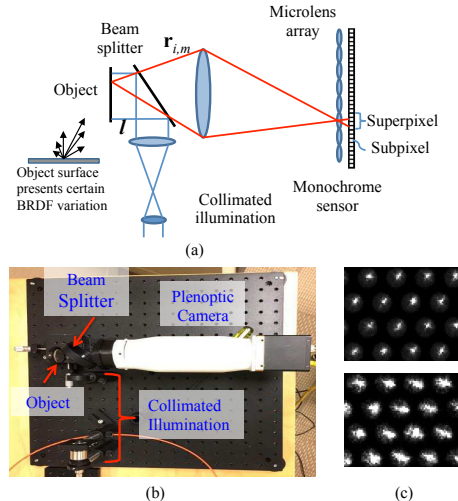


Figure 3. (a) Schematic diagram of our gonio-plenoptic imaging system. (b) Our Bench setup. (c) Raw sensor images captured on different materials: plastic (above) and copper-nickel (below).

onto a corresponding section of the sensor array and forms a superpixel. Therefore, the sensor array can be subdivided into superpixels and each superpixel is subdivided into subpixels. When the main lens is focused on the object each subpixel within a superpixel captures light from the same region of the object, but at different propagation angles.

In our system, the microlens has focal length of $700 \mu\text{m}$, diameter of $100 \mu\text{m}$, and F-number of 7. The microlenses are arranged in a hexagonal sampling pattern. The main lens has the optical characteristics of a low-power microscope with 50 mm focal length and working F-number of 10. Due to constraints imposed by the optical housing of our prototype the F-number of the main lens does not exactly match the F-number of the microlens. Therefore, we sacrifice some pixels that do not receive light behind each microlens, which can be observed as the big gap between neighboring superpixels as shown in Figure 1. The system has object space numerical aperture (NA) of 0.13, which has about $\pm 7^\circ$ cone of light entering the lens. The sensor is a 6600×4400 pixels monochrome CCD sensor, which is divided into about 90,000 superpixels and captures 2 frames per second. The microlens array is mounted directly on the CCD sensor. The effective resolution of the reconstructed height map is determined by the number of superpixels, which is 349×259 pixels. Under each superpixel there are about 130 effective subpixels. However, the number of effective pixels is reduced in the off-optical-axis region because of vignetting in the main lens. Each subpixel captures about 1.1° cone of light reflected from surface. The object is placed at the working distance of 52 mm of the main lens. The field of view of the camera is about $12.5 \text{ mm} \times 8.4 \text{ mm}$. The effective spatial resolution is determined by the number of superpixels and is about $36 \mu\text{m}/\text{superpixel}$.

Figure 3 (c) shows examples of raw sensor images captured on surfaces that are made of plastic and copper-nickel. Each superpixel captures the specular lobe of the reflection. It can be seen that the copper-nickel object causes a broader response than plastic. For a lot of materials the surface normals cannot be estimated directly from the location of superpixel peaks; therefore, a BRDF model is employed to model the superpixel response.

3.2. Surface Reconstruction

As shown in Figure 2 and Figure 3 the light captured by different subpixels within a superpixel depends on surface normal and the type of material. The response of the superpixel can be modeled by using a BRDF model. We adopt the Ward BRDF model [24] which was used in [6] for surface reconstruction using photometric stereo and in [5] for estimating the spatial-varying reflectance properties of a surface. The BRDF is modeled as

$$f(\mathbf{n}, \mathbf{l}, \mathbf{r}_{i,m}) = \frac{\rho_d}{\pi} + \frac{\rho_s e^{-(\tan \delta / \alpha)^2}}{4\pi \alpha^2 \sqrt{\cos \theta_i \cos \theta_r}}, \quad (1)$$

where \mathbf{n} and \mathbf{l} are unit vectors of surface normal and collimated illumination direction, $\mathbf{r}_{i,m}$ is the unit vector of the light field viewing direction of the i th subpixel in the m th superpixel, ρ_d and ρ_s are diffuse and specular reflection coefficients, α is a measure of surface roughness, θ_i and θ_r are illumination and camera viewing zenith angles, and δ is the angle between \mathbf{n} and the halfway vector \mathbf{h} that is between illumination and viewing directions. The parameters θ_i , θ_r and δ on the right side of Equation 1 as well as the halfway vector \mathbf{h} depend on the $\mathbf{n}, \mathbf{l}, \mathbf{r}_{i,m}$ vectors as follows. The angles θ_i and θ_r are defined in a local coordinate of the surface and are calculated based on these normal vectors as

$$\theta_i = \arccos(\mathbf{l} \cdot \mathbf{n}), \text{ and } \theta_r = \arccos(\mathbf{r}_{i,m} \cdot \mathbf{n}). \quad (2)$$

Similarly the halfway vector \mathbf{h} and δ are calculated as

$$\mathbf{h} = \frac{\mathbf{l} + \mathbf{r}_{i,m}}{\sqrt{|\mathbf{l} + \mathbf{r}_{i,m}|}}, \text{ and } \delta = \arccos(\mathbf{h} \cdot \mathbf{n}). \quad (3)$$

The \mathbf{l} and $\mathbf{r}_{i,m}$ vectors are known based on the system configuration. The ρ_d, ρ_s, α and \mathbf{n} are unknown parameters. There are two degrees of freedom among the three components n_x, n_y , and n_z in the surface normal unit vector \mathbf{n} , yielding a total of five unknown parameters to be solved. In our system the illumination vector is parallel to the optical axis. The $\mathbf{r}_{i,m}$ vector encodes the directional information of the light field captured by the i th subpixel in the m th superpixel. This corresponds to the mapping of the light field to the detectors. In an ideal case, the $\mathbf{r}_{i,m}$ vector is the same for all the superpixels. However, this is not the case in a real system. In our system, the mapping of the light field to the

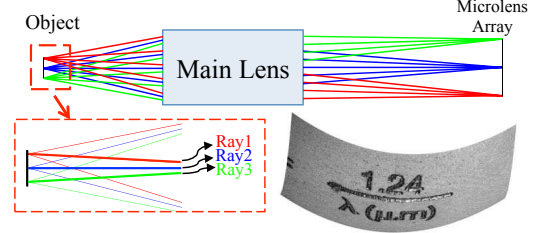


Figure 4. Ray-tracing simulation of our system and 3D rendering of a plastic ruler card surface without proper calibration.

detectors is determined by calibration, which accounts for imperfection of optics. We will present a novel object space calibration technique in the next section.

For each superpixel, the number of measurements equals the number of subpixels, which outnumbers the five unknown parameters. We estimate the unknown parameters for each superpixel using non-linear regression minimizing the following objective function

$$O_m(n_x, n_y, \rho_d, \rho_s, \alpha) = \sum_i [I_{i,m} - (\mathbf{l} \cdot \mathbf{n}) f(\mathbf{n}, \mathbf{l}, \mathbf{r}_{i,m})]^2. \quad (4)$$

where $I_{i,m}$ is the measurement of i th subpixel in the m th superpixel. This optimization process is repeated for each superpixel and yields surface normal, diffuse and specular reflection coefficients, and surface roughness per superpixel. In this paper the minimum of this objective function is solved using the Levenberg–Marquardt non-linear optimization algorithm. In our optimization, the initial value of the surface normal is selected as the halfway vector between the illumination direction and the viewing direction of a subpixel that has the highest response in a superpixel. The initial value of diffuse reflectance is set as the mean of subpixel values in each superpixel; the initial value of specular reflectance is set as the $\frac{1}{50}$ of the diffuse reflectance; and the initial value of surface roughness is set as 0.03. Since our system only captures light within $\pm 7^\circ$, we constrained the surface normal zenith angle to be within 20° . The surface height is then obtained based on the estimated surface normal. We adopt a commonly used approach to estimate the height field based on approximated gradient at each superpixel [6, 10].

3.3. Object Space Calibration

As shown in Equation 1 the viewing direction vector $\mathbf{r}_{i,m}$ for each subpixel in a superpixel needs to be known. However, determination of this viewing direction is highly dependent on the optical system and should be specified for each superpixel individually. To illustrate the dependency of the viewing direction on the superpixel location, a ray-tracing simulation of our system is shown in Figure 4. The three ray bundles are traced from the object to the microlens

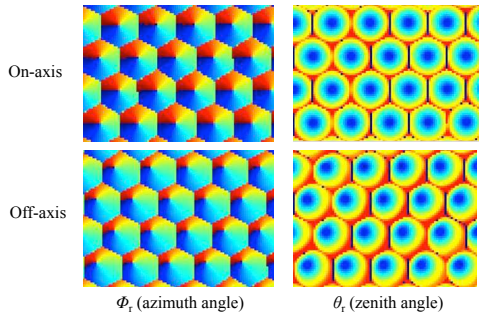


Figure 5. Calibrated light field mapping (azimuth and zenith angles) from object space to on-axis and off-axis superpixels.

array. Among these three ray bundles one passes through the microlens centered on the optical axis and the other two pass through off-axis microlenses. Ideally ray1,2,3 should propagate along the same direction and be parallel to each other, but due to the non-telecentricity of the optics in the object space those off-axis rays are significantly tilted. In addition to the object space non-telecentricity, vignetting as well as the image space non-telecentricity cause the rays' directions to be deviated from each other even further. An example of surface reconstruction without proper calibration is also shown in Figure 4, assuming the ray propagation directions are uniformly distributed within each superpixel. The card is flat, but the reconstruction shows a curved surface caused by the incorrect assumptions about the light field viewing directions.

In order to correct system distortions, we have developed an *object space calibration* to obtain a more accurate estimate of which light field coordinates map to which subpixels. It is called object space calibration because we trace the ray directly from the object space to each subpixel. This calibration process can be thought of an experimental ray-tracing in a real plenoptic imaging system. Ng's previous work [17] proposed a technique to digitally correct lens aberrations by tracing rays through optics based on a geometrically accurate model of the camera's lens. Differently our object space calibration does not require a model of lens. Instead, an experimental ray-tracing is performed, which enables us to characterize real systems including their manufacturing inaccuracies. In the experimental setup collimated light is reflected from a mirror placed in the object plane. The propagation direction of the light beam is controlled by tilting the mirror. We oriented the mirror along different zenith and azimuth angles and collected 72 calibration images, which are similar to the images shown in Figure 2. Each calibration image corresponds to the reflected light propagating along a known direction, and indicates which subpixels within each superpixel capture the light from that light field viewing direction. Since the directed light beam may expose more than one subpixel, the mapping of beam direction to sensor location is based on

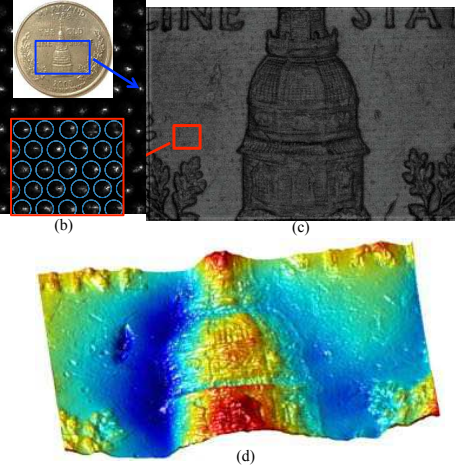


Figure 6. Reconstruction of Maryland quarter. (a) Original coin. (b) Zoomed in image of the sensor data. (c) Raw sensor image. (d) Surface reconstruction.

calculating a weighted centroid for the light captured within each superpixel. In order to create a mapping between viewing directions and discrete subpixels, a representative viewing vector for a specific subpixel is created via interpolation of viewing vectors mapped to neighboring centroids. The result is a mapping from the four-dimensional light field (x,y,u,v) to the subpixel. The calibration results for the on-axis and off-axis microlenses are shown in Figure 5. The mapped light field viewing direction is presented in a polar coordinate. The top two figures are mappings of azimuth angle and zenith angle, respectively, of light field viewing directions to on-axis superpixels, i.e., superpixels that are near the center of the sensor array. The warm color indicates a larger angle value and the cool color indicates a smaller angle. The point where all the colors meet in the azimuth angle map is the subpixel which captures the on-axis rays from the object. The bottom two figures are mappings of azimuth angle and zenith angle, respectively, of light field viewing directions to off-axis superpixels, i.e., superpixels that are near the edge of the sensor array. In a perfect telecentric case, both the on-axis and off-axis mapping would look the same. However, that is not the case here. The center point of the off-axis azimuth and zenith angle mapping is shifted relative to the center of the superpixels. The calibrated mapping is used as a known parameter, which is the viewing direction vector $\mathbf{r}_{i,m}$, in the BRDF model. A reconstruction of the same plastic ruler card but with object space calibration will be presented later in Figure 7.

4. Results

4.1. Experimental Results

We captured a single-shot on a Maryland quarter using our gonio-plenoptic imaging system. The original coin used

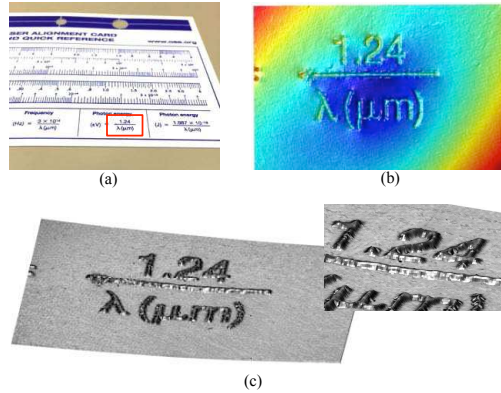


Figure 7. Surface reconstruction for a plastic ruler card. (a) The original ruler card used in the experiment. A single-shot was captured on the region within the red outline by using our system. (b) Reconstructed height map. (c) 3D rendering of the surface.

in our experiment and the raw sensor image are shown in Figure 6 (a), (b), and (c). Raw sensor data was captured on a small portion of the coin, which is indicated as the blue outline. Based on a single image the coin surface is reconstructed as shown in 6 (d). Even surface damage on the left side can be clearly seen in the reconstruction.

Figure 7 (a) shows the original plastic ruler card used in our experiment. A single-shot was taken on the region within the red outline by using our system. The raw sensor image was previously shown in Figure 1 (b). The height map and 3D rendered surface of this card are presented in Figure 7 (b) and (c). The height map has higher values in the upper-left and lower-right corners, which is due to the fact that the card was bended a little bit by the optic holder. Using the known camera parameter of our system we calculated the height of the blue ink from the reconstructed surface data to be $10 \mu\text{m}$. That height agrees with a digital micrometer measurement we took of the blue ink on the white card.

We further performed experiment on a surface with dynamic deformation. The experimental setup is shown in Figure 8. In the experiment a white card was used as the object. “ICCV” four letters were written on the back of the card, and video was captured on the front of the card using our prototype. Because the tip of ball pen pressed the back of the card, the front surface presented deformation. The front surface was still uniformly white while writing letters on the back, and the imprint caused by the press could not even be easily visualized. We captured video at 2 fps on the front surface while writing down letters. The data collection session only took about 30 seconds. The full video showing the reconstructed dynamic surface deformation is presented as supplementary material, and selected frames are shown in Figure 9. Based on our surface reconstruction, the height of the imprint was measured to be about $50 \mu\text{m}$.

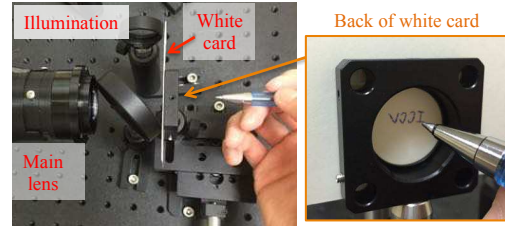


Figure 8. Setup of dynamic scene acquisition.

4.2. Accuracy Analysis

To evaluate the performance of our system a dielectrically coated concave spherical mirror from Thorlabs is used as the ground truth. The concave mirror has diameter of 25.4 mm and focal length of 75 mm, which gives a radius of curvature of 150 mm, and the center thickness is 6 mm. According to the manufacture the front surface irregularity of the concave mirror is less than $\lambda/4$ at 633 nm. The tolerance of the diameter is $+0.0/-0.2$ mm, and the tolerance of the thickness is ± 0.2 mm. Only a single image of the mirror was captured using our system, and the reconstructed height map is shown in Figure 10 (a). The height profile of the concave mirror measured based on the manufacture’s specifications is used as ground truth and is shown in Figure 10 (b). Please note that the plot does not present any manufacturing tolerance of the diameter and thickness. The height profile reconstructed based on our system is compared to the ground truth in Figure 10 (b). The root-mean-square error (RMSE) in depth between the estimated profile and ground truth is $5.3 \mu\text{m}$, which is about 4% of the total surface height. The mismatch between our reconstruction and the ground truth is due to either the manufacturing tolerance or the error introduced by our system. It can be seen that even though the concave mirror itself does not contain any texture we are still able to accurately reconstruct the shape with single-shot data acquisition.

4.3. Comparison with Prior Art

4.3.1 Simulation

Our gonio-plenoptic imaging system is compared to Wang and Dana’s scanning parabolic mirror approach [23] and Goldman et al.’s multi-illumination photometric stereo [6] based on simulations. The angular range, number of images acquired, sensor resolution, and data acquisition time of these two systems as well as ours are shown in Table 1. Detailed description of all these three systems can be found in the supplementary material. Our gonio-plenoptic imaging system was simulated with three different NA settings, and all these settings were with the same sensor size and the same number of subpixels per superpixel as described in Section 3.1. NA of 0.13 is the setting of our current prototype, which gives an angular range of $\pm 7^\circ$. NA of 0.21

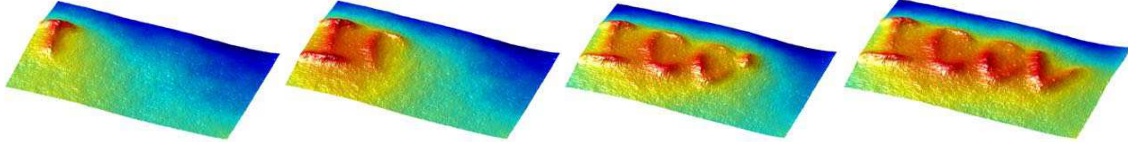


Figure 9. Reconstructed dynamic surface deformation of a white card. Full video is presented as supplementary material.

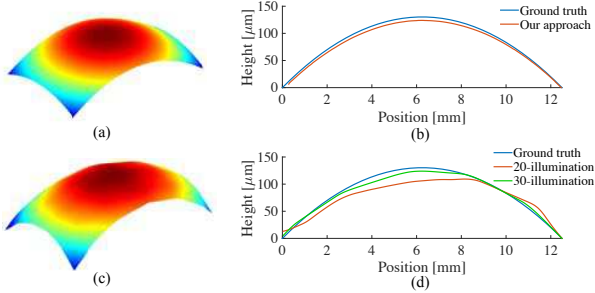


Figure 10. Accuracy analysis against the concave mirror. Reconstructed height map using (a) our system and (c) 30-illumination photometric stereo. Reconstructed height profile using (b) our system and (d) 20, 30-illumination photometric stereo.

is also the setting based on our current prototype but has matched main lens and microlens F-numbers, which gives an angular range of $\pm 12^\circ$. The matched F-number can be achieved by using larger housing for the main lens. NA of 0.34 is a setting if we use an objective lens with higher power, which gives an angular range of $\pm 20^\circ$. NA of 0.34 is a reasonable selection, and an off-the-shelf objective lenses with much higher NA is available. The angular range can be further increased if a higher NA is selected. The reconstructed height map resolution based on these three different systems is set as 200×200 pixels in order to be comparable with Wang and Dana’s system.

In the simulation a synthetic random surface with varied surface normals was first generated and was used as ground truth. Sensor images based on three different systems were then simulated. The reflection of the surface was assumed to be perfectly specular, and all the imaging system were also assumed to be perfect. Surface normal maps were estimated based on peaks of specular reflection lobes, and height maps were reconstructed based on surface normal maps. Two random surfaces with different surface normal ranges were used for simulation. One is with the surface normal zenith angle θ_s changed from 0° to 18° , and another one is with θ_s changed from 0° to 39° . The reconstructed height maps based on different systems are presented in supplementary material. Selected results of height map reconstruction for surface angle range $\theta_s \in [0^\circ, 39^\circ]$ are shown in 11, and the quantitative comparison is summarized in Table 1. The normalized root-mean-square error (NRMSE) is calculated against the ground truth surface height values. It is shown that Wang and Dana’s system

has the highest accuracy based on its much wider angular range and much denser angular sampling, but with the expense of acquiring a large amount of data (40,000 images with VGA resolution) and much longer data acquisition time (1 hour). Our system only requires a single-shot with 6600×4400 resolution and much shorter data acquisition time that is determined by camera exposure (20-100 milliseconds). In terms of total pixel counts our system is 413 time more efficient than Wang and Dana’s. Meanwhile, we still achieve reasonable accuracy compared to Goldman et al.’s 12-illumination approach. However, if a smaller NA is selected most steep structures are lost in our reconstruction. It is seen that with a larger NA much higher accuracy can be achieved. The simulation results show that with NA=0.34 the accuracy of our system is already comparable to Wang and Dana’s while using only milliseconds in data acquisition.

4.3.2 Real Experiment

In the real experiment we only compared our system to Goldman et al.’s multi-illumination photometric stereo approach [6]. In the multi-illumination setup we used a 3376×2704 pixels monochrome CCD sensor without microlens array, and a double telecentric lens from Edmund Optics, which ensures the system is orthographic. The object space NA of the lens is about 0.013, which has about 1.5° cone of light entering the lens, which is comparable to the angular sampling per subpixel of our gonio-plenoptic system. The field of view of the camera is about $12.5 \text{ mm} \times 10 \text{ mm}$, which is also similar to our system. The multi-illumination setup has much higher spatial sensor resolution, which is about $3.7 \mu\text{m}/\text{pixel}$. In order to compare the results with our system’s, we down-sampled the multi-illumination system sensor data to 338×271 pixels, which is similar to the spatial resolution of our system. The illumination used in this experiment is also collimated, and its zenith and azimuth angles were changed within $\pm 7^\circ$ and $\pm 180^\circ$ respectively. In [6] a total of 12 light sources were used for surface reconstruction. In our experiment we oriented the illumination in 20 and 30 different directions respectively, and took an image for each illumination direction. The surface normal map and height map were reconstructed using the same approach presented in Section 3.2, except that multiple camera viewing vectors $\mathbf{r}_{i,m}$ are substituted by multiple illumination vectors \mathbf{l}_i .

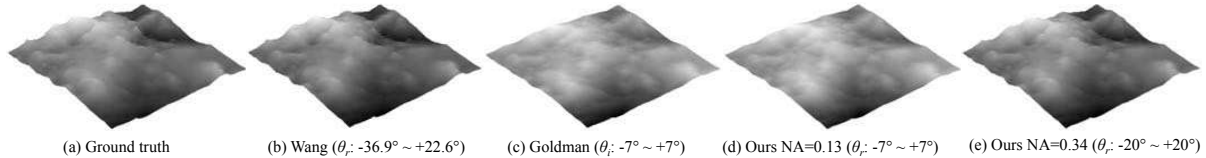


Figure 11. Comparison of surface reconstruction based on simulations ($\theta_s \in [0^\circ, 39^\circ]$). More results are shown in supplementary material.

Table 1. Quantitative comparison with Wang and Dana [23] and Goldman et al. [6] based on simulations.

Method	Wang and Dana	Goldman et al.		Our Gonio-plenoptic Imaging System			
				NA=0.13	NA=0.21	NA=0.34	
Angular range	$-36.9^\circ \sim +22.6^\circ$	$-7^\circ \sim +7^\circ$	$-20^\circ \sim +20^\circ$	$-7^\circ \sim +7^\circ$	$-12^\circ \sim +12^\circ$	$-20^\circ \sim +20^\circ$	
Number of images acquired	40,000	12		1			
Sensor resolution (pixels)	640×480	3072×2048		6600×4400			
Data acquisition time	1 hour	25 minutes		20-100 milliseconds			
NRMSE	$\theta_s=0^\circ \sim 18^\circ$	1.2%	16.4%	4.5%	11.5%	3.9%	1.5%
	$\theta_s=0^\circ \sim 39^\circ$	5.7%	15.9%	8.4%	14%	7.6%	6.1%

The reconstructed height map of the same concave mirror using 30-illumination photometric stereo is shown in Figure 10 (c), and the estimated height profiles using 20 and 30 illumination directions are shown in Figure 10 (d). The RMSE in depth between the 20-illumination measurement and the ground truth is $15.7 \mu\text{m}$, which is about 12% of the total surface height; and the RMSE for the 30-illumination measurement is $5.3 \mu\text{m}$, which is about 4% of the total surface height. It is seen that by using more illumination directions the estimated height profile is much closer to the ground truth. Our system generates less RMSE compared to the 20-illumination experiment, and has the same RMSE as the 30-illumination experiment, while performing only a single data acquisition. Compared to the multi-illumination approach our method reconstructs a much smoother height map. That is because in our system there are a large number of subpixels in each superpixel (about 130 for on-axis superpixels), and each subpixel samples the BRDF from a slightly different viewing angle. Therefore, we have much denser sampling of the BRDF variation within a finite camera viewing range. If more illumination directions are used in the photometric stereo approach the result will be less noisy and smoother, but it would take much longer for image acquisition and require a more complex setup. However, compared to the multi-illumination approach our system has limited effective surface normal reconstruction range as well as lower spatial resolution, as discussed in the conclusion section.

5. Conclusion

We presented a gonio-plenoptic imaging system that realizes single-shot specular surface reconstruction and can capture dynamic surface deformation in video mode. The system is comprised of a collimated illumination source and a plenoptic camera, which captures the BRDF variation of a surface. Based on a BRDF model the surface normals and height map can be reconstructed. In addition we intro-

duced a novel object space calibration technique that maps the four-dimensional light field reflected from the object directly to all the subpixels in each superpixel.

Our system has unique strengths and limitations. The system setup is simple and does not include any moving illumination or optical component. The system only needs to be calibrated once. The data acquisition is efficient because only one image is required for reconstruction. The reflectance properties of the surface are maintained since our system performs non-contact imaging and does not require an additional layer to be placed on the surface. Moreover, our system can capture dynamic surface deformation. However, in our system and the current implementation, there are some limitations. First, due to the limited NA our current prototype only captures about $\pm 7^\circ$ cone of light, which constrains the range of surfaces normals that can be reconstructed. Any reflected light out of this range will not be captured by our system. Thus, if the surface has very steep slopes we are not able to reconstruct the surface normals and our method only works for relief surfaces. In our current prototype due to constraints on the optical housing, the main lens F-number does not match the microlens F-number, and therefore we lose light that comes from wider angles. If we have matched F-numbers $\pm 12^\circ$ range can be achieved. A much larger NA can be further selected to overcome this limitation as shown in the simulation results. Second, the spatial resolution is reduced by using the plenoptic camera because the effective resolution is determined by the number of microlenses. A larger sensor with smaller pixels and microlens with smaller diameter can be used to enhance the spatial resolution. Third, our method will fail if the surface is Lambertian, and finding the range of BRDFs for which the method works will be our future work.

Despite these limitations, our system provides a simple and efficient way to capture the geometry of a specular surface, which is suitable for applications in computer vision.

References

- [1] E. H. Adelson and J. Y. A. Wang. Single lens stereo with a plenoptic camera. *IEEE Trans. PAMI*, 14(2):99–106, 1992. 1, 2
- [2] R. Basri, D. Jacobs, and I. Kemelmacher. Photometric stereo with general, unknown lighting. *International Journal of Computer Vision*, 72(3):239–257, 2007. 2
- [3] T. Chen, M. Goesele, and H.-P. Seidel. Mesostructure from specularity. In *Proc. CVPR*, pages 1825–1832, 2006. 2
- [4] Y. Francken, T. Cuypers, T. Mertens, J. Gielis, and P. Bekaert. High quality mesostructure acquisition using specularities. In *Proc. CVPR*, pages 1–7, 2008. 2
- [5] A. Gardner, C. Tchou, T. Hawkins, and P. Debevec. Linear light source reflectometry. In *ACM Trans. Graph.*, number 3, pages 749–758. ACM, 2003. 2, 3.2
- [6] D. B. Goldman, B. Curless, A. Hertzmann, and S. M. Seitz. Shape and spatially-varying BRDFs from photometric stereo. *IEEE Trans. PAMI*, 32(6):1060–1071, 2010. 1, 2, 3.2, 3.2, 4.3.1, 4.3.2, 1
- [7] A. Hertzmann and S. M. Seitz. Example-based photometric stereo: Shape reconstruction with general, varying BRDFs. *IEEE Trans. PAMI*, 27(8):1254–1264, 2005. 1, 2
- [8] Y. Ji, J. Ye, and J. Yu. Reconstructing gas flows using light-path approximation. In *Proc. CVPR*, pages 2507–2514, 2013. 2
- [9] H. Jin, S. Soatto, and A. J. Yezzi. Multi-view stereo beyond Lambert. In *Proc. CVPR*, pages I–171–I–178, 2003. 2
- [10] M. K. Johnson and E. H. Adelson. Retrographic sensing for the measurement of surface texture and shape. In *Proc. CVPR*, pages 1070–1077, 2009. 1, 2, 3.2
- [11] M. K. Johnson, F. Cole, A. Raj, and E. H. Adelson. Microgeometry capture using an elastomeric sensor. *ACM Trans. Graph.*, 30(4):46:1–46:8, July 2011. 1, 2
- [12] M. Levoy, R. Ng, A. Adams, M. Footer, and M. Horowitz. Light field microscopy. *ACM Trans. Graph.*, 25(3):924–934, July 2006. 2
- [13] M. Levoy, Z. Zhang, and I. McDowall. Recording and controlling the 4d light field in a microscope using microlens arrays. *Journal of Microscopy*, 235(2):144–162, 2009. 2
- [14] A. Lumsdaine and T. Georgiev. The focused plenoptic camera. In *Proc. ICCP*, pages 1–8, 2009. 2
- [15] C. Ma, X. Lin, J. Suo, Q. Dai, and G. Wetzstein. Transparent object reconstruction via coded transport of intensity. In *Proc. CVPR*, pages 3238–3245, 2014. 2
- [16] S. K. Nayar, A. C. Sanderson, L. E. Weiss, and D. A. Simon. Specular surface inspection using structured highlight and gaussian images. *IEEE Trans. Robot. Autom.*, 6(2):208–218, 1990. 2
- [17] R. Ng. *Digital light field photography*. PhD thesis, Stanford University, 2006. 3.3
- [18] R. Ng, M. Levoy, M. Brédif, G. Duval, M. Horowitz, and P. Hanrahan. Light field photography with a hand-held plenoptic camera. *Tech. rep., Stanford University*, 2005. 2
- [19] F. Pernkopf and P. O’Leary. Image acquisition techniques for automatic visual inspection of metallic surfaces. *NDT & E International*, 36(8):609–617, 2003. 1
- [20] C. Perwaß and L. Wietzke. Single lens 3D-camera with extended depth-of-field. In *IS&T/SPIE Electronic Imaging*, pages 829108–829108, 2012. 1, 2
- [21] B. C. Platt and R. Shack. History and principles of Shack-Hartmann wavefront sensing. *Journal of Refractive Surgery*, 17(5):S573–S577, 2001. 2
- [22] I. Tosic and K. Berkner. Light field scale-depth space transform for dense depth estimation. In *Proc. CVPRW*, pages 441–448, 2014. 1
- [23] J. Wang and K. J. Dana. Relief texture from specularities. *IEEE Trans. PAMI*, 28(3):446–457, 2006. 1, 2, 4.3.1, 1
- [24] G. J. Ward. Measuring and modeling anisotropic reflection. *Computer Graphics*, 26(2):265–272, 1992. 3.2
- [25] G. Wetzstein, D. Roodnick, W. Heidrich, and R. Raskar. Refractive shape from light field distortion. In *Proc. ICCV*, pages 1180–1186. IEEE, 2011. 2
- [26] R. J. Woodham. Photometric method for determining surface orientation from multiple images. *Optical Engineering*, 19(1):191139–191139, 1980. 2
- [27] T. Yu, N. Xu, and N. Ahuja. Recovering shape and reflectance model of non-lambertian objects from multiple views. In *Proc. CVPR*, volume 2, pages II–226–II–233, 2004. 2